Journal of Science: Advanced Materials and Devices 10 (2025) 100870

Contents lists available at ScienceDirect

Journal of Science: Advanced Materials and Devices

journal homepage: www.elsevier.com/locate/jsamd

Research Article

Corona triode poling of P(VDF-TrFE) nanofibers: Mechanisms and optimization strategies

Leonardo Gasperini [*], Giacomo Selleri [**], Davide Pegoraro, Daniele Mariani, Alberto Rumi, Paolo Seri, Davide Fabiani

Department of Electrical, Electronic, and Information Engineering, University of Bologna, Viale Risorgimento 2, 40136, Bologna, Italy

ARTICLE INFO

Keywords:
Corona poling
Piezoelectric
P(VDF-TrFE) nanofibers
Factorial design

ABSTRACT

The effectiveness of the poling process of poly(vinylidene fluoride-trifluoroethylene) (P(VDF-TrFE)) nanofibers is essential for their use in engineering applications (i.e., artificial piezoelectric skins, self-sensing composite materials). While traditional contact poling methods present electrical breakdown risks through the highly porous nanofibrous membranes, the corona poling technique offers a non-contact alternative, utilizing ion generation to polarize piezoelectric materials without direct interaction between the high-voltage electrode and the sample. The corona poling process is well-established for P(VDF-TrFE) thin films, but literature lacks a reliable methodology for P(VDF-TrFE) nanofibers. This study addresses this gap by systematically investigating the differences between the corona poling of P(VDF-TrFE) films and nanofibers and aims to disclose the distinct physical mechanisms involved. First, the corona triode setup is optimized for P(VDF-TrFE) films, achieving a piezoelectric strain coefficient d_{33} of 23 pC N^{-1}. The parameters of the corona setup are then methodically recalibrated for the nanofiber's polarization, with the rationale behind these adjustments discussed and validated through experimental investigations. Such a refined corona poling method leads to a d_{33} equal to −20.8 pC N^{-1} for the nanofibers, contemporary allowing for a comprehensive understanding of the physical mechanisms behind the two distinct methods.

1. Introduction

In recent years, the rapid development of multifunctional materials has accelerated the transition towards the use of smart components for industrial and wearable applications, such as flexible electronics or self-sensing composite materials [1–3]. Among them, piezoelectric materials feature an intrinsic energy conversion mechanism, which paves the way for a variety of self-sensing materials with autonomous power supply [4,5]. Since the piezoelectric effect locally converts mechanical energy into electrical energy, piezoelectric sensors have been increasingly used to accurately measure pressure, acceleration and force changes in various applications [6,7]. Among them, the high piezoelectric performances of piezo-ceramics materials have been widely exploited in various fields, such as accelerometers, structural health monitoring (SHM) systems and self-sensing composite structures [8–11].

Alternatively, piezoelectric polymers attracted enormous interest in the last decades, due to their great flexibility and processability [12]. Poly (vinylidene fluoride) (PVDF) and its copolymer with trifluoroethylene P(VDF-TrFE) are the most widespread piezoelectric polymers, and they can be used to monitor bending [13–16], twisting, finger tapping [17] and for energy harvesting purposes [18,19]. Furthermore - via electrospinning technique - piezoelectric polymers can be fabricated in the shape of nanofibers, whose high flexibility can be exploited for wearable applications, such as soft electronic skins (e-skin) [20,21], or tactile sensors [22–24]. Thanks to their high porosity, nanofibers can be also embedded into hosting matrix to develop of self-sensing materials with special shapes or curvilinear structures, such as prosthetic soles, robotic hands, and pressure sensors [25–27]. In addition to their piezoelectric functionalization, numerous studies have demonstrated the positive influence of nanofiber interleaving on the mechanical properties of composite materials [28,29].

Since P(VDF-TrFE) generally presents low piezoelectric performances, a poling process is required to achieve higher sensitivity before to be used for sensing or energy harvesting applications. Starting from

---

[*] Corresponding author.
[**] Corresponding author.

E-mail addresses: leonardo.gasperini@unibo.it (L. Gasperini), giacomo.selleri2@unibo.it (G. Selleri).

https://doi.org/10.1016/j.jsamd.2025.100870
Received 17 January 2025; Received in revised form 20 February 2025; Accepted 23 February 2025

the early 1990s, several studies have been performed on the poling phenomena to align the dipoles of the material crystal lattice [30,31]. Traditional poling methods involve the use of a high-voltage electrode and a ground electrode which are put in contact with the sample, generating a high electric field across the specimen thickness, both using DC or AC voltage [32,33]. However, during the polarization of nanofibers, several issues may arise due to the presence of air voids within the nanofibrous membrane, which can initiate an electrical breakdown avalanche. To mitigate this, the nanofibrous mat is often polarized after being embedded into a hosting matrix [20,25,34]. The primary drawback of this approach is the uneven distribution of the applied electric field between the piezoelectric phase and the filler matrix, depending on the electrical properties of the two phases [10,25]. This disparity can significantly reduce the electric field experienced by the piezoelectric phase, thereby limiting the piezoelectric response of the composite material.

Promising strategies exist for the alternative polarization of nanofibers before the integration within the composite material, avoiding electric breakdowns risks. For instance, highly sensitive piezoelectric membranes have been fabricated by aligning the dipoles using a peculiar electrospinning procedure [35], or by polarizing them in an oil bath with high dielectric strength, which can subsequently be removed [36].

Alternatively, a non-contact poling method such as the corona technique could represent an effective and non-disruptive way to induce permanent polarization on the piezoelectric material. When a sufficiently high potential difference is established between a fine wire electrode and a plate, the surrounding air is ionized, and the generated ions flow towards the ground base. By placing the piezoelectric film on top of the ground electrode, ions will deposit onto its surface and induce the movement and orientation of dipoles [37]. This technique has already attracted significant interest in the field of polymer film poling, as reported for PVDF films [38–40], or for $Bi_{0.95}Ba_{0.05}Fe_{0.95}Zr_{0.05}O_3$ (BBFZO) incorporated in PVDF [41]. Moreover, the corona poling method can also be applied on composite metamaterials with 3D shapes, enhancing the piezoelectric response compared to the traditional DC contact poling method. In these materials, the use of corona poling allows to apply high electric field to the piezoelectric phase limiting the risk of electrical breakdown [42–44]. However, the attainment of a uniform polarization on the whole sample surface is challenging, which is why a significant improvement has been made with the so-called corona triode technique.

This method involves the use of a metallic grid placed between the high-voltage electrode and the ground plate to achieve a more uniform distribution of the electric field within the deposition area, hence a better surface charge distribution. The effects of poling time and grid voltage were investigated in PVDF film using Fourier transform infrared spectroscopy (FTIR) and direct measurement of piezoelectricity [45]. Meanwhile, Giacometti et al. employed a constant current corona triode method for charging nonlinear optic (NLO) polymers and PVDF foils [46,47]. Instead of using a metallic grid, Li et al. set up a meandering path for the movement of the high voltage needle controlled by a robotic arm, to uniform the ion distribution [48].

As far as corona poling on nanofibers is concerned, exiguous works in literature provide detailed polarization procedures and they focus on few parameters, such as the voltage values to be applied to the needles and the grid [49–51]. Owing to the intrinsically porous nature of nanofibrous mats, the ion deposition mechanism responsible for polarization differs significantly from that of thin-film polarization.

This study bridges this gap by elucidating the different physical processes involved during the corona poling of P(VDF-TrFE) thin films or nanofibers, identifying the corresponding corona triode configurations that optimize the piezoelectric strain coefficient d_{33}. In addition to the systematic investigations of the two distinct mechanisms, this work provides guidelines for tailoring the desired d_{33}, supported by in-depth analyses of the influence of each parameter in the corona triode technique. First, a Design of Experiment (DoE) [52] approach was adopted to identify the optimal poling conditions for a commercial thin film of P(VDF-TrFE), by studying the effects of the variety of parameters involved in the corona triode technique (i.e., temperature, geometrical and electrical parameters). Starting from these findings, the corona triode method was systematically readjusted for the polarization of P(VDF-TrFE) nanofibers produced via electrospinning, thus offering a comprehensive understanding of the two distinct mechanisms.

2. Experimental

The manufacturing process of P(VDF-TrFE) nanofibers and the features of the commercial P(VDF-TrFE) film are first described in Section 2.1. The corona polarization apparatus used in this work is shown in detail in Section 2.2, with a particular focus on the parameters that are involved in the process. The methods to measure the charge deposition on the sample surface and the corona current distribution are described in Section 2.3 and Section 2.4, respectively. The former method is employed to have feedback on the impact of certain parameters, i.e., the presence or absence of the grid and the number of needles, on the corona poling process. Finally, Section 2.5 reports the electromechanical and chemical analyses performed on the piezoelectric specimens, before and after poling.

2.1. Sample preparation

Commercial P(VDF-TrFE) films (40 × 40 × 0.02 mm) were kindly provided by Solvay S.p.A. Milan.

The P(VDF-TrFE) nanofibrous mats were manufactured via electrospinning starting from a polymeric solution, prepared by dissolving the piezoelectric copolymer (P(VDF-TrFE)80/20 mol%, $M_w = 600$ kDa, Curie temperature $T_c = 133$ °C, provided by Solvay S.p.A. Milan) in dimethylformamide (DMF) and acetone (AC). The polymeric solution (7 wt% P(VDF-TrFE), 23 wt% DMF, and 70 wt% AC) was magnetically stirred for 3 h to fully dissolve the polymer. The electrospinning process was performed with a Spinbow Lab Unit (Spinbow S.r.l., Bologna, Italy) and comprises a needle connected to a high voltage generator (HVDC Spellman SL10-60 kV) set at 14 kV. The nanofibers were collected on a low-speed rotating drum (165 rpm) connected to the ground and placed 15 cm from the needle. The process took place for 6 h to obtain a nanofibrous mat with a thickness equal to 80 μm and a grammage of 45 g m^{-2}.

The electrospun nanofibers were analyzed using a Phenom Pro X scanning electron microscope (SEM). Prior to the micrographs, one sample was cut in a nitrogen bath for the cross-section examination, and all the samples were sputter-coated with gold. The average diameter was evaluated on 100 nanofibers using an image analysis software (ImageJ).

2.2. Corona poling

Corona discharge is a phenomenon that occurs when a high voltage is applied to an asymmetric electrode configuration, such as point-to-plane geometry. The gas that fills the gap between the electrodes is subjected to a divergent electric field, especially in the proximity of the tips. The local electric stress incepts a collisional process between available free charge carriers and the surrounding neutrals, unleashing a large number of ionic species, strongly dependent on the applied voltage and medium. This restricted area around the needle is named ionization region, whereas the confining region that extends towards the ground plate is called drift or conduction zone. When a dielectric layer is introduced in between the high voltage electrode and the ground plane, free carriers are able to reach and deposit onto the surface of the insulation. This produces an accumulation of electrostatic charges (positive or negative, depending on the experimental conditions), which in turn produces an electric field opposite to the imposed one. Such a process will proceed until a balance in between the local electric field in the gaseous region and that created by the deposited charges is achieved is achieved. Under this steady state condition, the polarization of the dielectric has occurred, accomplishing the so-called “corona poling”.

As aforementioned, a metallic grid could be interposed between the high voltage electrode and the ground plate to homogenize the ion distribution all over the sample surface [53].

Since the effectiveness of the corona poling technique hinges on a variety of parameters, a peculiar in-house-built cell was fabricated to study different conditions (see Fig. 1). In particular, a brass support was manufactured to hold up to 25 needles, with a grid pattern of 5 × 5 (vertical and horizontal spacing of 10 mm). Moreover, the possibility to vary the needle-to-grid (D_{ng}) and the grid-to-ground (D_{gg}) distances was included in the cell design. To compare the corona triode technique with the gridless corona poling method, a removable copper grid (mesh dimensions 1 × 1 mm^2) was adopted. The supporting structure of the poling cell was made of PTFE, to electrically insulate the high-voltage region with the grid and the ground plate, as shown in Fig. 1. The polarization setup included two high-voltage (HV) generators, as schematically represented in the equivalent electric circuit of Fig. 1. One HV generator was connected to the brass needle holder and the other to the metallic grid. The piezoelectric specimen was placed above the aluminum plate connected to the ground. An auxiliary resistor (R_{aux}) of 2.1 MΩ was added in parallel to the grid to limit the capacitive coupling between the HV needles and the grid. The effects of the geometric parameters (D_{ng} and D_{gg}) together with the HV values applied on the grid (V_g) and the needles (V_n) were investigated by means of two factorial designs, so as to optimize the piezoelectric strain coefficient d_{33}. In addition, the effect of the poling temperature was also evaluated with the One Factor At Time (OFAT) method. The full description of these methods is provided in Section 3.3.

2.3. Electrical charge distribution

Since the working mechanism of the corona poling relies on the deposition of the electric charges on the piezoelectric sample surfaces, in this work the electrical charge distribution has been measured for different corona poling conditions. The measurements were performed after the corona poling process using a 20-kV electrostatic voltmeter (TREK, model 341B) [54,55]. A non-contact probe (TREK, model 3455 ET) was coupled with the electrostatic voltmeter to perform the surface potential tests. The probe was clamped to a custom 3-axis motorized positioning stage with a resolution of 0.1 mm. Immediately after the polarization process, the ground plate of the corona cell - where the specimen was placed - was removed and fixed below the probe, as shown in Fig. 2. The distance between the probe sensing element and the piezoelectric sample was set to 5 mm. Electrostatic potential mapping was performed by monitoring the potential while the probe followed a predefined motion pattern at a constant speed over the entire surface of the polarized specimen. The entire scanning process took about 30 s to cover a 60 × 60 mm^2 area, and the resulting 2D map was reconstructed during post-processing.

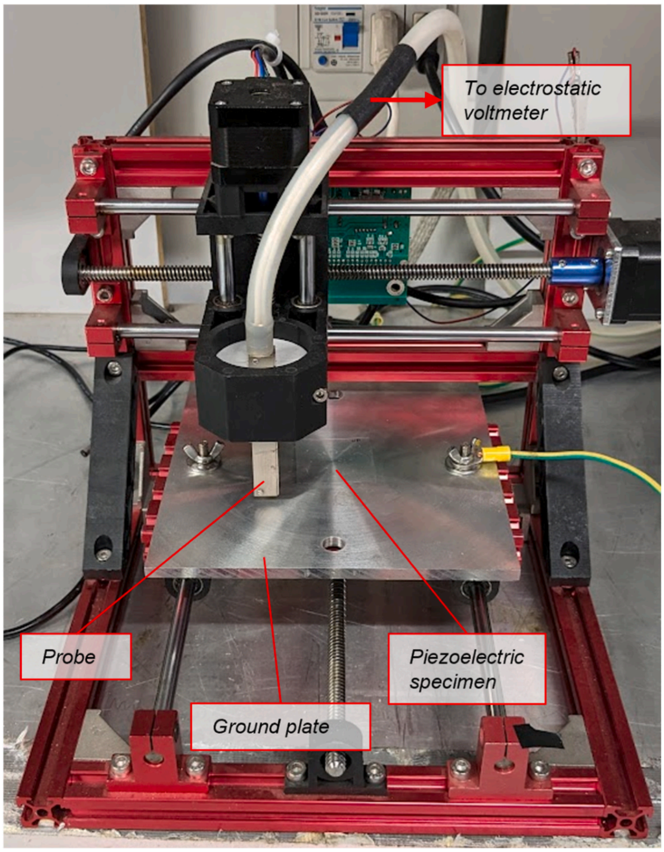

Fig. 2. Charge distribution measurement setup.

The output of the electrostatic voltmeter is a surface potential, which is strictly correlated to the amount of electrical charges deposited on the specimen surface during the corona polarization process. The surface potential values were acquired by an oscilloscope (Tektronix DPO 5034B, digital phosphoric oscilloscope) and correlated to the position of the probe pattern. This setup was exploited for different corona poling conditions. In particular, the effect of the number of needles (n_n equal to 1, 9 or 25) was considered, as well as the presence or the absence of the metallic grid. The D_{ng} and the D_{gg} were fixed at 30 mm and 10 mm, respectively. The voltage applied to the needles V_n was equal to 20 kV,

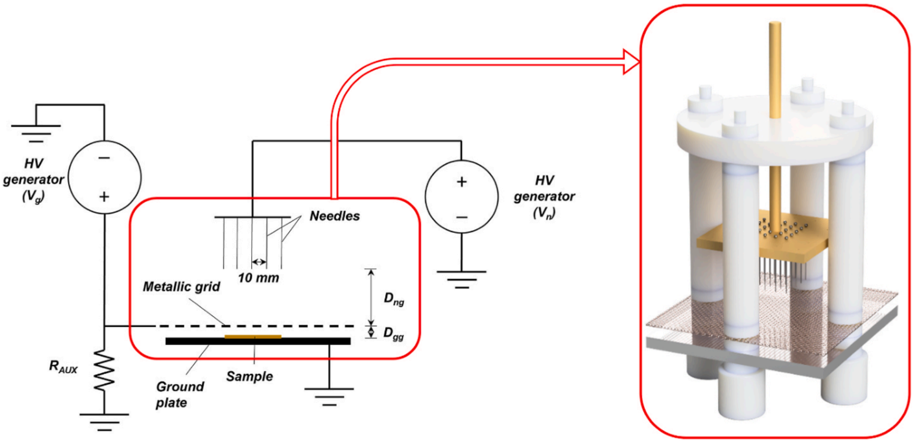

Fig. 1. Equivalent circuit for the polarization process and corona triode poling cell with 25 needles.

while the high voltage of the grid V_g was set to 3 kV. The same configurations were repeated by applying a negative voltage value, both to the needles and the grid.

2.4. Corona current density measurement

Current density measurements were performed for different geometrical configurations to observe the behavior of the inception voltage and the maximum applicable voltage prior to electrical discharge [56–58]. The study of the current density distribution, which is involved during the corona polarization process, is a suitable method to investigate the polarization efficiency. The ground plate of the cell described in Section 2.2 was replaced with a current measuring system equipped with a guard ring, as shown in Fig. 3, to detect only the current crossing the bulk insulation of the sample. The central aluminum cylinder was fabricated with the same area of the piezoelectric specimens used in this study (16 cm^2) and it worked as a probe to measure the current flowing the thickness of the specimen. The current probe was electrically insulated from the ground plate through a PTFE circular crown (inner diameter 55 mm outer diameter 65 mm) and it was connected to an electrometer (Keithley 6517B) to measure the current. The neighboring metal region was grounded to remove the leakage current (Fig. 3).

The analyses were carried out by varying the number of needles (1, 9, and 25) and the distance (d) between the tip and the ground plane (30, 35, and 40 mm). For each configuration, the voltage was increased from zero to the maximum applicable voltage before breakdown.

The same current measurement setup was replicated in the case of a negative voltage source. These further measurements were performed to better exacerbate how polarity affects the corona discharge process.

2.5. Piezoelectric characterization

The piezoelectric strain coefficient d_{33} of the poled specimens was measured by using a piezometer (d_{33} PiezoMeter System, Piezotest, Singapore, www.piezotest.com), by applying a sinusoidal oscillating force of 0.25 N at 110 Hz. The d_{33} coefficient was calculated as the average of five measurements performed on the surface of the piezoelectric sample, and the standard deviation value provides information about the uniformity of the d_{33} of each specimen.

In Appendix A, the piezoelectric signals are also reported as response of a compressive sinusoidal force oscillating between 0 N and 80 N, before and after poling both for P(VDF-TrFE) films and nanofibers. The measuring setup consists of a linear motor (LinMot) equipped with a 300 N load cell (Model 1042, Tedea-Huntleigh), and the output voltage was measured by an electrometer (Keithley 6517B, input impedance >200 TΩ), according to the equivalent piezoelectric circuit described in Ref. [25]. Moreover, accelerated life cycle fatigue tests have been performed on the polarized P(VDF-TrFE) films and nanofibers, as reported in Appendix A.

Wide-angle X-ray diffraction (WAXD) analyses were conducted on the treated samples by means of X'PERT pro Instrument equipped with a 1-D PIXcell using CuKα radiation (40 mA, 40 kV). The measurements were performed at room temperature in 2θ range of 10 °C–80 °C, with a step size of 0.033° and time/step of 20 s. WAXD was employed to evaluate the crystallinity of the P(VDF-TrFE) films and nanofibrous mats before and after poling, as reported in Appendix B. To determine the β-phase content of the samples, Fourier Transform Infrared (FTIR) spectroscopy (PerkinElmer Spectrum II) was performed in attenuated total reflectance (ATR) mode to analyze the chemical composition of the specimens. The ATR-FTIR spectra were recorded in a wavenumber range of 4000-450 cm^{-1} (Appendix B).

3. Results and discussion

Prior to the detailed description of the results of the polarizations performed on the P(VDF-TrFE) films and on the nanofiber mats, investigations on the optimal configuration of the corona triode setup are reported. In particular, the preliminary tests were focused on the effect of the number of needles and the presence of a metallic grid. The number of needles was changed to analyze the current, which is involved in the process, as described in Section 3.1. The homogeneity of the charge distribution on the sample surface was evaluated through the insertion and the removal of the metallic grid between the needles and the ground plate, both with numerical simulations and experimental surface potential tests (Section 3.2).

Based on the aforementioned evaluations, the experimental campaign was first developed on the P(VDF-TrFE) films (Section 3.3). The poling temperature was first studied using the OFAT method, while two factorial designs were proposed to study the impact of the geometrical and electrical parameters (factors: D_{ng}, D_{gg}, V_g and V_n). The optimization of such parameters was exploited for subsequent studies on the piezoelectric nanofibrous mats, as reported in Section 3.4. The impact of each factor was evaluated by measuring the piezoelectric strain coefficient d_{33}, both for P(VDF-TrFE) films and nanofibers.

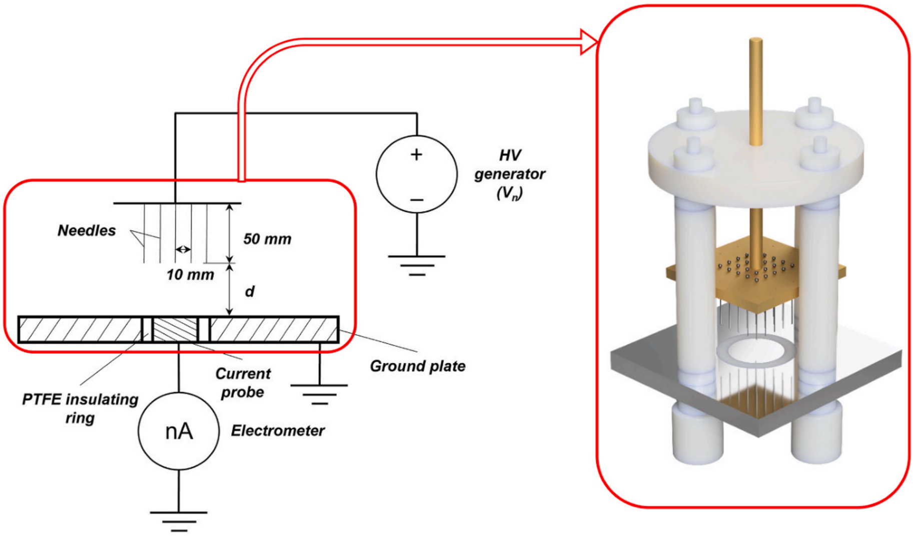

Fig. 3. Equivalent electric circuit and corona cell for current measurement.

3.1. Current-voltage curves

The current-voltage curves for the three different needles-ground distances (*d*) defined in Section 2.4 are reported in Fig. 4, both for positive and negative voltage sources.

In the case of positive currents, the distance d is the parameter that mostly affects the high voltage limit before electrical breakdown (e.g., 20 kV for $d = 30$ mm and 27 kV for $d = 40$ mm). Moreover, for a fixed voltage value, the corona current is higher for lower distances between the needles and the ground. At 20 kV, the current generated by 25 needles placed at $d = 30$ mm (Fig. 4a) is equal to 164 μA, whereas it decreases to 25.4 μA and 16.8 μA for $d = 35$ mm and $d = 40$ mm (Fig. 4b and c). This trend remains evident when examining the maximum applicable voltage for the three different configurations. In all cases, the highest current value is always measured for $d = 30$ mm, regardless of the number of needles used. On the other hand, the number of needles used for the corona current generation does not affect the breakdown voltage value, but strongly influences the measured current. Across all configurations, employing 25 needles consistently led to higher current values.

The usage of a negative voltage source results in a substantially lower absolute current measured on the ground electrode compared to the corresponding positive values at a fixed voltage level, as clearly visible in the graphs of Fig. 4d, e, f. For instance, in the case of a configuration with $d = 30$ mm, 25 needles and an applied voltage differential of 20 kV, the measured current with negative polarity is reduced by 47%, compared to the value obtained with a positive voltage supply. Moreover, with negative polarity, the breakdown of the air gap occurs for higher voltage values.

These trends suggest that negative corona poling leads to a lower charge generation, likely due to a higher dispersion of the negative species along the air path between the needles and the ground due to their much higher mobility, compared to positive carriers.

3.2. Charge distribution analysis

The deposition mechanism of the electric charges is responsible for the poling of the sample of the P(VDF-TrFE) film. To achieve a constant piezoelectric response all over the sample surface, the electric species generated by the corona discharge should homogeneously deposit on the specimen surface. This aspect is investigated in this section by varying the corona poling conditions (i.e., number of needles and presence of the grid), both in terms of numerical simulations (Section 3.2.1) and surface potential measurements (Section 3.2.2).

3.2.1. Current density simulations

This section aims to qualitatively describe current density flow by modeling the Laplacian electric field distribution of each setup.

Numerical simulations (software Comsol Multiphysics) were conducted under different poling conditions to evaluate the distribution of the current density J on the surface of the P(VDF-TrFE) film. Charge generation mechanisms and chemical reactions typical of corona discharge physics will not be considered here.

The poling setup was varied by including different numbers of needles (i.e., 1, 9 and 25), by varying the distance between the needles and the ground plate, and by adding a metallic grid, as shown in the left side of the panel of Fig. 5. The voltage applied to the needles and the grid can be found in Section 2.3.

Fig. 5 reports values of current density normalized to the minimum value J_0, which is calculated on the whole sample surface for each poling condition. In particular, the graphs refer to the J/J_0 ratio calculated on the segment AB (line in the middle of the sample) of the piezoelectric film, while the corresponding maps provide a graphical view of the current density on the whole sample surface.

When the needle-ground distance is equal to 1 cm (first row of the panel), a highly uneven distribution of the current density is observable with a single needle, where J/J_0 reaches 12 in the central region of the specimen. The use of 9 or 25 needles mitigates this effect, though significant variations remain evident in both the graphs and the corresponding surface maps. A more uniform J distribution is achieved by increasing the needle-ground distance to 4 cm (second row of the panel in Fig. 5). However, some inhomogeneity persists in the center of the sample surface, where J/J_0 exceeds 1. The final row of the panel illustrates the poling conditions with the insertion of the metallic grid between the needles and the ground. In these cases, J/J_0 is uniformly equal to 1 along the AB segment.

These qualitative results clearly suggest that the addition of the metallic grid can significantly enhance the uniform distribution of electric charges on the sample surface, thus leading to homogeneous polarization all over the piezo-polymer surface.

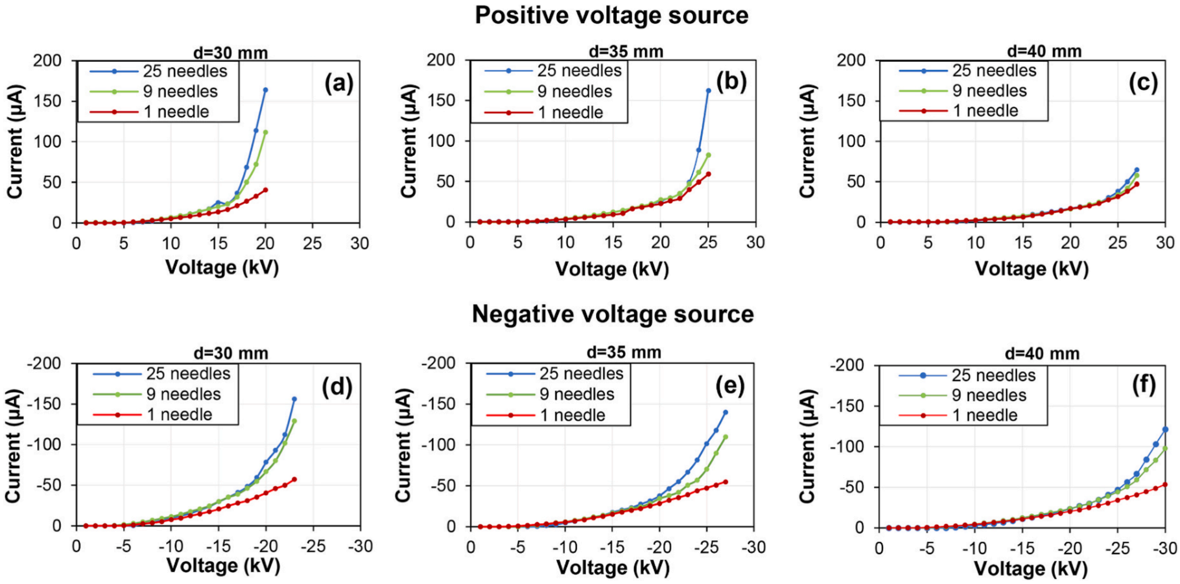

Fig. 4. Current-voltage curves with positive source for a) 30 mm, b) 35 mm and c) 40 mm of distance between the needles and the ground plate. The same configurations are repeated for the negative voltage source d), e), f).

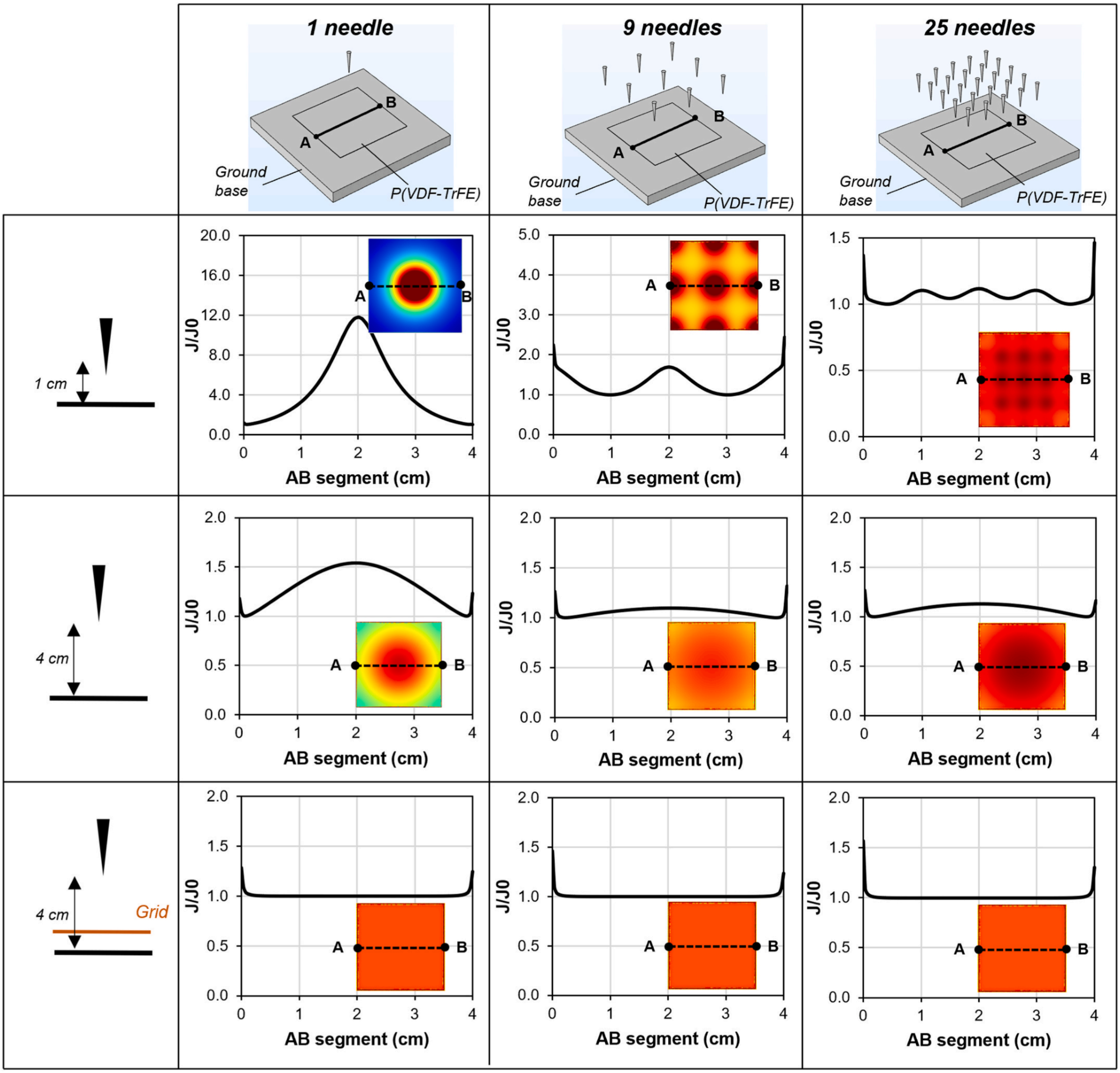

Fig. 5. Normalized current density values calculated via numerical simulation on the segment AB of the surface of the P(VDF-TrFE) samples, for different setup conditions.

3.2.2. *Charge mapping*

The surface potential maps displayed in Fig. 6 aim to provide information about the electrical charge distribution under corona-triode and corona-gridless configurations, both for positive and negative high-voltage sources, as described in Section 2.3. On each map, the black-filled circles indicate the presence and the position of the needles used for each corona poling configuration. Since the probe movement itself caused a small drift of electrostatic charges on the sample surface, results were post-processed to confer the potential maps the original rectangular shape of the specimens [59].

Fig. 6a reports the surface potential 2D maps in the case of positive high-voltage. The first row refers to the gridless poling configurations. In this case, mottled surfaces are observable both for 1, 9 and 25 needles. In particular, the use of 1 and 9 needles led to an extremely irregular surface charge distribution, with high-voltage values located in isolated spots of the 2D maps. This trend was mitigated in the 25 needles griddles configuration, even if some potential differences are still observable. On the other hand, the presence of the grid allowed to improve the uniformity of the 2D potential maps for each needle configuration, consistently with the numerical simulations of Section 3.2.1. Moreover, the presence of the grid enhanced the deposition of electric charges on the sample surfaces, due to the addition of another high-voltage source. Among all the poling configurations, the 2D map corresponding to the corona triode poling with 25 needles is the most uniform one and presents the highest surface potential values.

Fig. 6b displays the surface potential maps after a negative corona polarization process. Similarly to Fig. 6a, the top row representing gridless poling exhibits an extremely non-uniform charge distribution on

(a) Positive potential surface maps

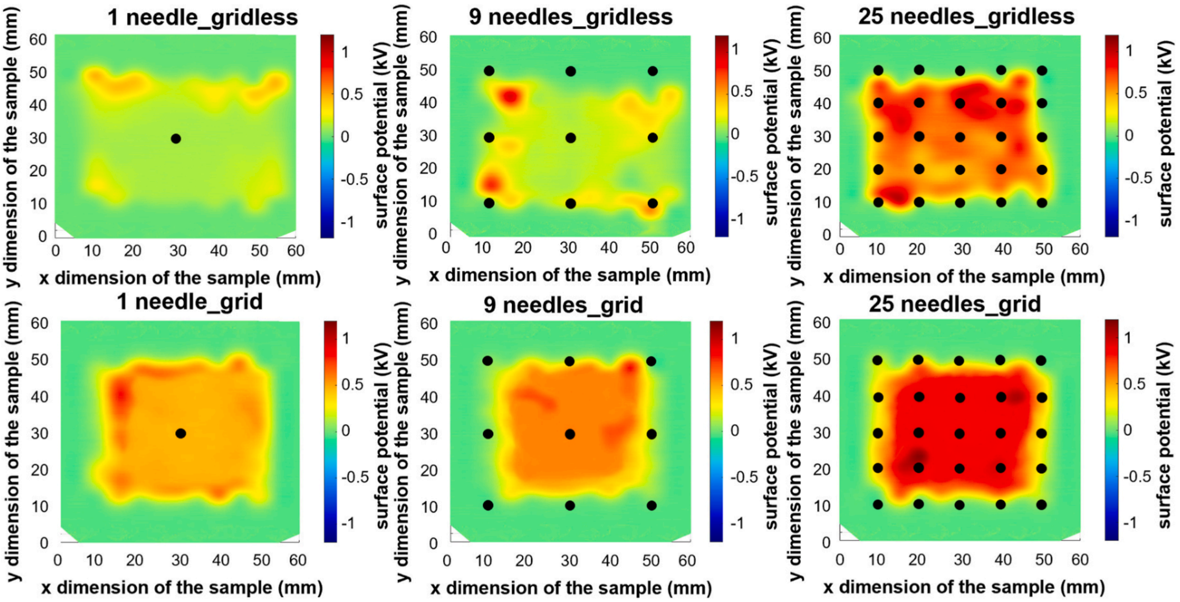

(b) Negative potential surface maps

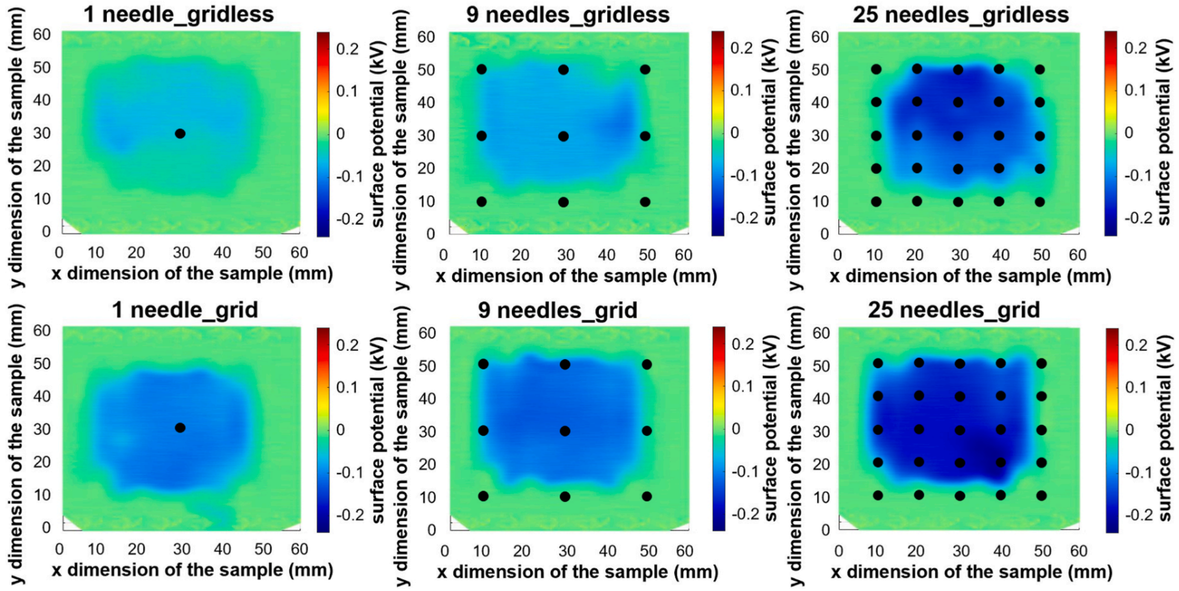

Fig. 6. a) Positive potential surface maps, b) Negative potential surface maps.

the sample surface, with a rise in the surface potential in the 25-needles case. As in the case of positive high-voltage sources, the presence of the metal grid yields 2D maps with an enhanced uniformity of the surface potential distribution.

Nevertheless, the assessed surface potential of the 2D negative maps is substantially lower than that of the positive ones, as discernible in the color bars. This disparity is attributable to the distinct mechanism governing the negative corona discharge. Specifically, the reduced mass of the electrons involved in this process engenders a heightened degree of instability of the process. Consequently, these electrons tend to disperse over a broader spatial domain, resulting in a restricted portion of them which is collected on the sample surface. On the contrary, the positive ions of the positive corona poling flow from the needles to the ground electrode in a more defined area, leading to higher values of surface charge distribution. This result is also justified by the findings of current measurements shown in the previous chapter.

3.3. *Film polarization*

As demonstrated in Section 3.2, the presence of the grid remarkably improves the homogeneity of the potential distribution on the surface of the samples. Therefore, the following investigations were carried out using the corona triode method, with 25 needles.

Due to the high number of parameters involved in the corona triode polarization method, a strategy to lighten the experimental campaign on the piezoelectric P(VDF-TrFE) commercial films was properly tuned to preserve the robustness of the results. Three main steps were identified: first, the poling temperature effect on the polarization was evaluated with the One Factor At Time (OFAT) method (Section 3.3.1). Afterwards, two factorial designs were adopted to evaluate the effect of the distances (DoE with two variation levels for the factors D_{ng} and D_{gg}) and the high voltage values (DoE with four variation levels for the factors V_n and V_g), in Section 3.3.2 and Section 3.3.3, respectively. Additionally, poling processes with negative polarity have been conducted to assess the behavior of P(VDF-TrFE) films under negative voltage corona discharge (Section 3.3.4).

3.3.1. OFAT

Initially, the OFAT method was adopted to investigate the impact of the temperature on the polarization process of the P(VDF-TrFE) commercial films. The other parameters involved in the poling process were held to fixed values ($D_{ng} = 30$ mm, $D_{gg} = 10$ mm, $V_n = 20$ kV, $V_g = 4$ kV and $n_n = 25$). Before starting the corona discharge, the sample was placed in an oven for 30 min to ensure a homogeneous distribution of the set poling temperature. Each poling test was conducted at a specific poling temperature, which varied between 30 and 130 °C with a temperature-step of 20 °C. As observable in Fig. 7, the piezoelectric film polarized at 30 °C presents the highest d_{33} (20.8 pC N^{-1}), while increased poling temperature values led to lower d_{33}. This trend could be likely attributed to the higher conductivity of the P(VDF-TrFE) films for increasing temperatures, which favor the charge migration toward the ground plate. On the contrary, at T = 30 °C, the period of time that the charges remain on the surface is longer, thus improving the polarization effectiveness.

Therefore, the subsequent analyses on the other parameters involved in the corona poling of commercial films were conducted at 30 °C.

3.3.2. Factorial design: distances

A 2^k factorial design with two factors (k = 2) implies four polarization tests, where D_{ng} and the D_{gg} were varied according to Table 1. The voltage of the needles V_n was fixed at 20 kV, the voltage of the grid at 3 kV and the poling time was 60 min. For each configuration, the d_{33} is reported in the third column of Table 1, together with the standard deviation value.

The highest d_{33} value (20.82 pC N^{-1}) was measured in correspondence of $D_{ng} = 30$ mm and $D_{gg} = 5$ mm, which is the configuration where the distances are the smallest.

These results are visually represented in the response surface graph of Fig. 8a. In Pareto's diagram of Fig. 8b, the factors and the interaction between them are associated with a standardized effect (SE). The factor that impacts the most on the d_{33} value is the distance between the grid and the ground D_{gg}, while the variation of D_{ng} is considerably less relevant, but still higher than the reference line of statistical significance at 95% probability (red line of Fig. 8b). This is well in line with what should be expected, since a variation of D_{gg} has a direct impact on the electric field imposed on the specimen surface, which in turn directly determines the amount of deposited superficial charges. On the other hand, D_{ng} is more related to the number and kinetic energy of ionic species, having an indirect impact on deposited charges. Moreover, the interaction between D_{gg} and D_{ng} is just lower than the line of significance, as visible in the Pareto's chart. This peculiarity also finds a correspondence in the almost absence of curvature of the response surface graph. These evidences allow to affirm that the interaction between the two factors is negligible, while the impact of each of them influences the final piezoelectric response.

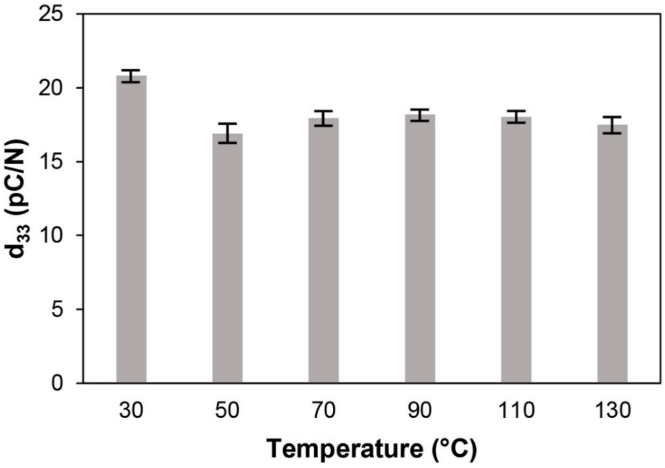

Fig. 7. OFAT analysis of d_{33} by varying the poling temperature.

Table 1
2^2 factorial design for distances evaluation.

D_{ng} (mm)	D_{gg} (mm)	d_{33} (pC N^{-1})
30	5	20.82 ± 1.15
35	5	19.70 ± 1.01
30	10	15.70 ± 0.96
35	10	12.11 ± 1.69

3.3.3. Factorial design: voltages

In accordance with the insights presented in Section 3.3.2 regarding the distances used in the corona triode, the investigations on the voltages applied to the needles and the grid were performed in two steps. The D_{gg} was fixed at 5 mm, as it is the most impactful parameter of the Pareto's chart of Fig. 8b; whereas two factorial designs were proposed by fixing $D_{ng} = 30$ mm and $D_{ng} = 35$ mm.

For both the D_{ng} values, a full 4^k factorial design was proposed, with k = 2 (V_n and V_g). However, since the distance between the needles and the ground limits the maximum applicable voltages before breakdown, the levels range of V_n are different for the two factorial designs. In particular, in the 30 mm-D_{ng} case the four levels of V_n are 14, 16, 18 and 20 kV, while in the 35 mm-D_{ng} case the V_n values are set at 16, 18, 20 and 22 kV. In both cases, the V_g levels are equal to 1, 2, 3 and 4 kV. The poling time was set at 60 min, the number of needles was 25, and the poling temperature was equal to 30 °C.

The d_{33} values obtained in the factorial design with $D_{ng} = 30$ mm are reported in Table 2 (left part), and their visual representation is shown in the response surface and Pareto's diagram of Fig. 9a. From the response surface graph of Fig. 9a, a curvature is detectable, which can be ascribed to the interaction between the two factors. This is also evident in the Pareto's diagram of Fig. 9a, where the SE is higher than the significance level. Nevertheless, the prominent factor is the voltage applied to the grid V_g, and the highest d_{33} can be found for $V_g = 20$ kV and $V_n = 4$ kV ($d_{33} = 23.01 \pm 0.92$ pC N^{-1}). This corroborates what was found in the previous chapter, being that parameters relative to grid conditions have a direct impact on deposited superficial charges, hence d_{33}, while parameters relative to needles have an indirect influence on results.

For the 35 mm-D_{ng} case, the d_{33} values are reported in Table 2 (right part). Based on the response surface graph of Fig. 9b, the curvature of the response surface is lower than the one of Fig. 9a, which indicates a smaller interaction between the factors under consideration. Indeed, as indicated by the Pareto's diagram (Fig. 9b), this interaction does not attain statistical significance. On the contrary, both the factors V_g and V_n substantially influence the d_{33}, which reach the highest value when the maximum voltage is applied to both the grid ($V_g = 4$ kV) and the needles ($V_n = 22$ kV), resulting in a $d_{33} = 22.20 \pm 0.50$ pC N^{-1}.

Considering both the configurations ($D_{ng} = 30$ mm and $D_{ng} = 35$ mm), it can be generally assumed that the most important parameter is V_g, while the level of significance of V_n slightly decreases for higher distances between the needles and the grid (SE = 5.25 for $D_{ng} = 30$ mm and SE = 5 for $D_{ng} = 35$ mm).

3.3.4. Negative corona triode

The experimental campaign based on the OFAT approach and two-factorial designs facilitated an investigation into the effects of various parameters involved in the corona triode method, with the aim of maximizing the piezoelectric strain coefficient d_{33} of the commercial P(VDF-TrFE) film. It is important to note that all tests on piezoelectric films were conducted using positive voltage sources, based on findings from the 2D surface potential maps shown in Fig. 6.

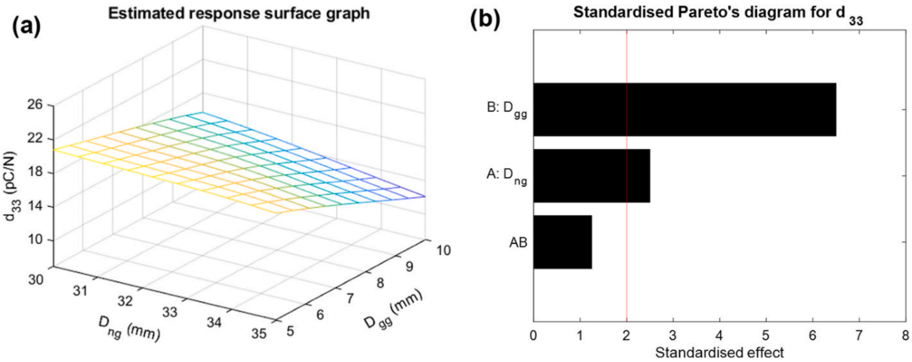

Fig. 8. a) Response surface graph and b) Pareto's diagram based on the D_{gg} and D_{ng} factors.

Table 2
4^2 factorial design for the voltages evaluation for $D_{ng} = 30$ mm (left part). 4^2 factorial design for the voltages evaluation for $D_{ng} = 35$ mm (right part).

$D_{ng} = 30$ mm			$D_{ng} = 35$ mm		
V_g (kV)	V_n (kV)	d_{33} (pC N^{-1})	V_g (kV)	V_n (kV)	d_{33} (pC N^{-1})
1	14	5.12 ± 0.48	1	16	12.15 ± 0.59
	16	5.93 ± 0.73		18	12.61 ± 0.83
	18	6.36 ± 1.07		20	13.05 ± 1.13
	20	6.98 ± 0.88		22	13.55 ± 1.20
2	14	8.61 ± 1.18	2	16	15.95 ± 1.02
	16	9.24 ± 1.43		18	16.56 ± 0.61
	18	9.54 ± 0.94		20	17.44 ± 1.36
	20	10.08 ± 1.96		22	17.96 ± 1.24
3	14	11.92 ± 0.97	3	16	16.39 ± 0.64
	16	13.20 ± 0.80		18	17.72 ± 0.79
	18	15.76 ± 1.90		20	20.06 ± 0.49
	20	21.18 ± 0.44		22	20.25 ± 1.39
4	14	10.22 ± 1.10	4	16	19.01 ± 0.73
	16	12.76 ± 0.94		18	19.58 ± 0.88
	18	17.00 ± 0.72		20	21.28 ± 1.14
	20	23.01 ± 0.92		22	22.20 ± 0.50

To assess the film behavior under negative voltage sources, P(VDF-TrFE) films were polarized under negative voltage conditions, as detailed in Table 3. By varying V_g from −1 kV to −4 kV, V_n was set to its maximum value before electrical breakdown, for both $D_{ng} = 30$ mm and $D_{ng} = 35$ mm. During the negative corona discharge, the broader spatial domain allows negative species to travel further, enabling an increase of V_n, which reaches a substantially higher absolute value than that achieved with positive corona (refer to Table 2 and Fig. 4). Despite this higher absolute V_n value, the resulting d_{33} remain significantly lower than those obtained with the positive corona triode. This outcome suggests that, although the increase of V_n, fewer electric charges deposit on the sample surface during negative corona discharge, as corroborated by the 2D surface maps of Section 3.2.2.

3.4. Nanofibers polarization

3.4.1. Poling mechanism

The setup that maximizes the piezoelectric strain coefficient d_{33} of the P(VDF-TrFE) commercial film was replicated for the nanofibrous membrane polarization, based on the considerations made in Section 3.3. Therefore, as a first attempt, the corona triode polarization was performed with the following conditions: 25 number of needles (n_n), poling time of 1 h, T = 30 °C, $D_{gg} = 5$ mm, $D_{ng} = 30$ mm, $V_g = 4$ kV, $V_n = 20$ kV (condition "a" of Table 4). However, with these parameters, no polarization was obtained and the d_{33} value was null.

This effect originates from the intrinsically different nature of a P(VDF-TrFE) nanofibrous membrane with respect to a P(VDF-TrFE) film. As visible in the SEM cross-section of Fig. 10a and in the top view of Fig. 10b, the nanofibrous membrane presents an extremely high porous grade, characterized by the presence of multiple interconnected air channels. It is worth highlighting that this study is related to nanofibrous mats with a diameter of 431 ± 72 nm (average diameter calculated with ImageJ) and a grammage equal to 45 g m^{-2}. Variations in these parameters may influence the size of the air pores, thereby affecting polarization efficiency. However, the primary objective of this paper is to investigate the different mechanisms of electric charge deposition in comparison to homogeneous films. When nanofibers are placed on the ground electrode of the corona poling cell, the positive ions generated from the corona needles can easily flow through the air pores of the piezoelectric membrane without depositing on its surface, thus preventing polarization. Subsequently, the poling setup has been readapted to address this issue, by adopting modifications which aim to increase the residence time of the electric charges on the piezoelectric nanofibers. First, to favor the dipole mobility of the crystalline lattice of the nanofibers, the poling temperature was increased up to the Curie temperature (130 °C). In this way, even if the electrons of the negative corona discharge reside for a short time on the nanofibers before flowing to ground, they can still contribute more effectively to the dipole alignment (condition "b" of Table 4, with $V_g = 3$ kV and $V_n = 16$ kV as maximum values before breakdown). In addition, a dielectric barrier of poly-coated paper was interposed between the nanofibers and the ground electrode, to preclude the charges from going directly towards the ground plate (condition "c" of Table 4). Finally, the positive voltage generators connected to the needles and the grid were replaced with negative HV sources. This modification is related to the high electronegativity of the fluorinated polymer, which renders the P(VDF-TrFE) attractive to negative charge carriers and rejective to positive ions. As a result, negative charges tend to remain longer on the P(VDF-TrFE) nanofibers than positive ones, since they are affected by the intrinsic attraction of the polymer, as represented in Fig. 10c and d. It is worth highlighting that also in commercial bulky films the electronegativity of the polymer has a role in the attraction of the negative charges on its surface, but the decreased density of negative species results in lower polarization level. This aspect is well endorsed by the negative current-voltage curves of Fig. 4, the negative 2D surface potential maps of Fig. 6b (see Section 3.2.2) and the d_{33} coefficients obtained with negative HV sources (see Section 3.3.4).

Starting from the same condition of P(VDF-TrFE) film polarization (condition "a" of Table 4), each change was inserted one at a time to systematically monitor the piezoelectric response, as summarized in Table 4. The geometrical parameters D_{ng} and D_{gg} were kept constant. Overall, the d_{33} present values close to zero except for conditions "c" and "g". Condition "c" resulted in $d_{33} = 2.6$ pC N^{-1}, but the combination of high temperature, poly-coated paper as dielectric barrier and negative HV sources (condition "g") led to a drastic increase of the d_{33} value up to −16.2 pC N^{-1}.

(a) D_{ng}=30 mm

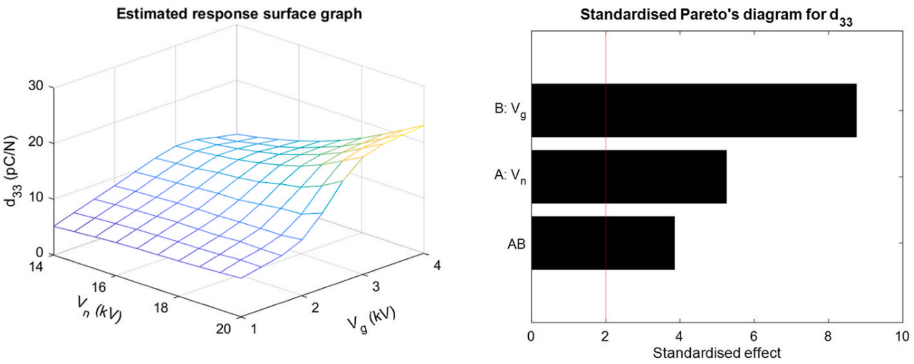

(b) D_{ng}=35 mm

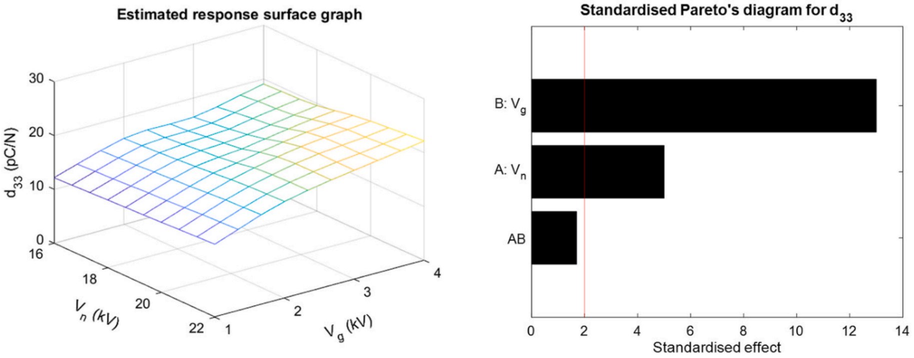

Fig. 9. a) Response surface graph and Pareto's diagram based on the V_g and V_n factors (D_{ng} = 30 mm). b) Response surface graph and Pareto's diagram based on the V_g and V_n factors (D_{ng} = 35 mm).

Table 3
P(VDF-TrFE) thin film poling with negative HV sources.

D_{ng} = 30 mm			D_{ng} = 35 mm		
V_g (kV)	V_n (kV)	d_{33} (pC N^{-1})	V_g (kV)	V_n (kV)	d_{33} (pC N^{-1})
−1	−28	−7.2 ± 2.1	−1	−29	−4.4 ± 1
−2	−28	−7.4 ± 2.4	−2	−29	−7.1 ± 2.3
−3	−28	−8 ± 1.6	−3	−29	−8.2 ± 1.3
−4	−28	−12.8 ± 0.5	−4	−29	−11 ± 0.5

Table 4
Corona poling of P(VDF-TrFE) nanofibers under different conditions.

	D_{gg} (mm)	D_{ng} (mm)	V_g (kV)	V_n (kV)	T (°C)	poly-coated paper	d_{33} (pC N^{-1})
(a)	5	30	+4	+20	30	no	10×10^{-3}
(b)	5	30	+3	+16	130	no	12×10^{-3}
(c)	5	30	+3	+16	130	yes	2.6
(d)	5	30	−4	−20	30	no	−9 x 10^{-3}
(e)	5	30	−3	−20	130	no	-16×10^{-3}
(f)	5	30	−4	−20	30	yes	-22×10^{-3}
(g)	5	30	−3	−20	130	yes	−16.2

3.4.2. Parameters optimization

Since the negative corona discharge involves lower current density than the positive one, the poling conditions (i.e., geometrical parameters and HV source amplitudes) were further studied to optimize the d_{33} of the P(VDF-TrFE) nanofibers. First, the experimental campaign focused on the optimization of the geometrical parameters. Similarly to the factorial design performed for the film polarization (see Section 3.3.2), different nanofibers-polarization setups were adopted by varying D_{ng} and D_{gg}, as shown in the bar graph of Fig. 11a. V_g and V_n were set at their maximum value before electric breakdown (i.e., the higher D_{ng} and D_{gg}, the higher the voltage values). In correspondence of the lower distances (D_{ng} = 30 mm and D_{gg} = 5 mm), the d_{33} is considerably higher than the other configurations, despite the lower values of V_g and V_n.

To assess the piezoelectric response under different high voltage polarization values, the most performing geometrical configuration (D_{ng} = 30 mm and D_{gg} = 5 mm) was further explored for a wider range of V_g and V_n values. V_g was equal to −1, −2 and −3 kV, while V_n was varied between −16 kV and −28 kV, as shown in Fig. 11b. For all the V_g values, the d_{33} follows a monotonous increasing trend with V_n. Similarly to the results obtained with the P(VDF-TrFE) films (Section 3.3), the voltage applied to the grid V_g has a remarkable impact, both in terms of amplitude and surface homogeneity. Indeed, for V_n = -28 kV the d_{33} rises from −13.2 pC N^{-1} for V_g = -2 kV up to −20.8 pC N^{-1} for V_g = -3 kV, which is a value comparable with the d_{33} of the commercial films. Additionally, for V_g = -3 kV the standard deviation is also considerably reduced with respect to polarization performed with V_g = -1 kV and V_g = -2 kV.

4. Conclusion

This work aims to systematically investigate the different mechanisms governing the corona poling of P(VDF-TrFE) in the shapes of thin film or nanofibers. Initially, polarization of P(VDF-TrFE) films was optimized by evaluating various corona triode parameters, achieving a piezoelectric strain coefficient d_{33} of 23 pC N^{-1}. The focus then shifted

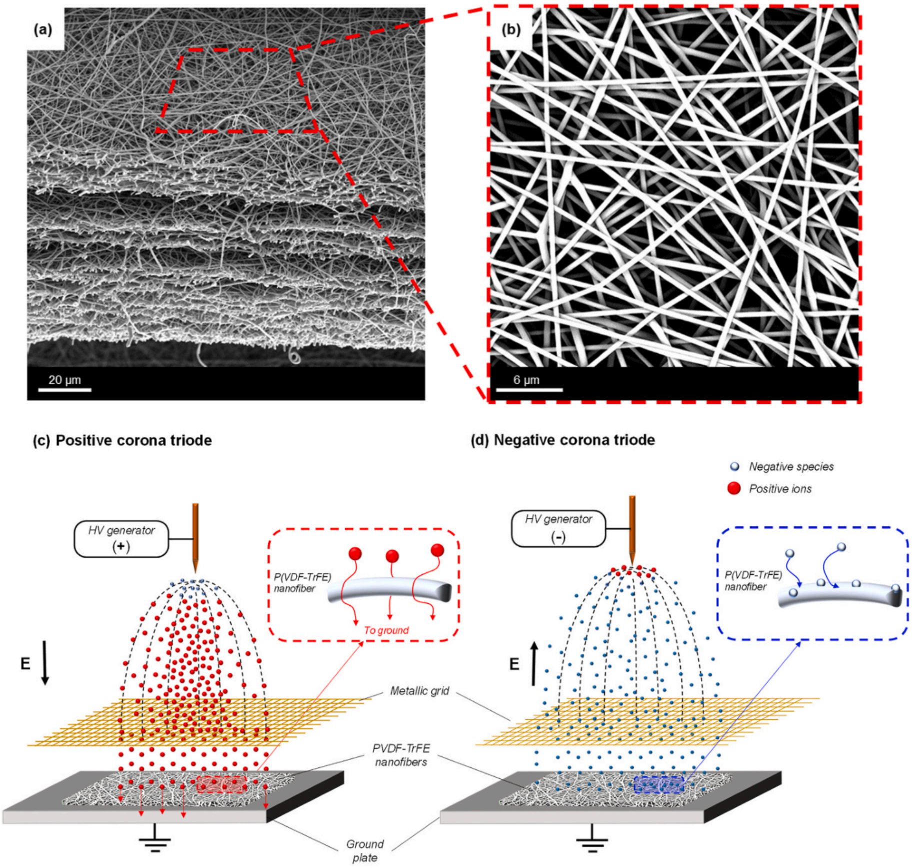

Fig. 10. SEM images of the P(VDF-TrFE) nanofibrous membrane in a) cross-section and b) top view; c) positive ions and negative species flowing mechanism in case of positive and d) negative corona poling of nanofibers.

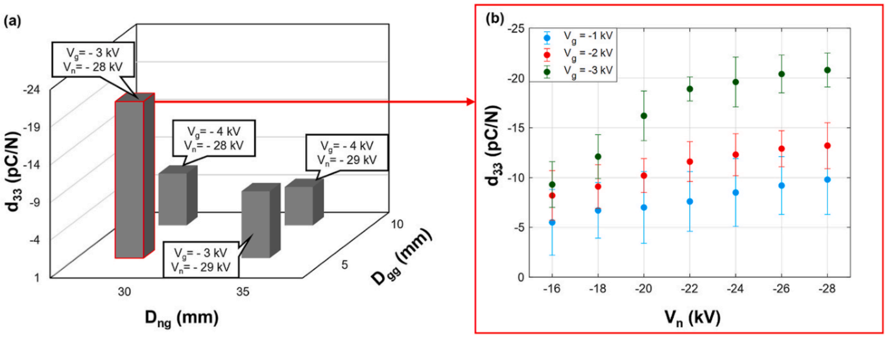

Fig. 11. d_{33} values of the nanofiber membranes for different a) D_{ng} and D_{gg} and b) V_n and V_g.

to the distinct mechanisms governing the corona poling of P(VDF-TrFE) nanofibers. Unlike films, nanofibrous membranes, characterized by their porous structure, allow corona discharge ions to pass through air voids without depositing on the fibers, thereby hindering polarization. Starting from the optimized film polarization setup, adjustments were systematically introduced and validated for nanofibers. Specifically, negative high-voltage sources replaced the positive corona discharge used for films. Despite the instability and reduced ion migration in the negative configuration, successful polarization was achieved due to the strong affinity of electrons for the electronegative fluorinated polymer. Additionally, the process was enhanced by increasing temperature to improve dipole mobility and by interposing a poly-coated paper between the nanofibers and the ground electrode to delay electron neutralization. These combined measures enabled effective polarization of nanofiber mats, achieving a d_{33} value of -20.8 pC N^{-1}. Herein, the systematic investigations performed on the corona triode poling represent a novel framework both for achieving high d_{33} of P(VDF-TrFE) nanofibers and for comprehensively clarifying the physical differences relative to film polarization. Additionally, the experimental campaign offers valuable guidelines for tailoring the d_{33} by tuning corona triode parameters. The proposed system has potential applications in industrial contexts and scaled-up systems, offering a feasible solution for the poling of larger-sized samples.

CRediT authorship contribution statement

Leonardo Gasperini: Writing – original draft, Methodology, Investigation, Formal analysis, Conceptualization. **Giacomo Selleri:** Writing

– original draft, Methodology, Investigation, Formal analysis, Conceptualization. **Davide Pegoraro:** Methodology, Investigation, Formal analysis. **Daniele Mariani:** Writing – original draft, Methodology, Conceptualization. **Alberto Rumi:** Methodology, Investigation, Conceptualization. **Paolo Seri:** Writing – original draft, Methodology, Investigation, Formal analysis, Conceptualization. **Davide Fabiani:** Writing – review & editing, Supervision, Conceptualization.

Declaration of competing interest

The authors declare that they have no known competing financial interests or personal relationships that could have appeared to influence the work reported in this paper.

Acknowledgements

The authors would like to thank Solvay and especially Alessio Marrani for providing the piezoelectric polymer. This work was supported by THOR - lighTweight self-cHarging piezO-supercapacitoR systems by nanotechnologies (Portable Charges for Soldiers) - NATO Science for Peace and Security Programme, under grant agreement G5772.

Appendix A

The piezoelectric signal before and after polarization are reported in Figure A.1, both for the P(VDF-TrFE) films and nanofibers membranes. The poling conditions are the ones which maximize the d_{33}, both for film and nanofibers. The specimens were mechanically compressed with a sinusoidal force oscillating between 0 N and 80 N at a frequency of 2 Hz and sandwiched between two copper tape electrodes with an aera of 1 cm^2. In Table A.1 the peak-to-peak output voltage, the d_{33} and the sensitivity are reported. The sensitivity was calculated as the ratio between the peak-to-peak output voltage and the force amplitude.

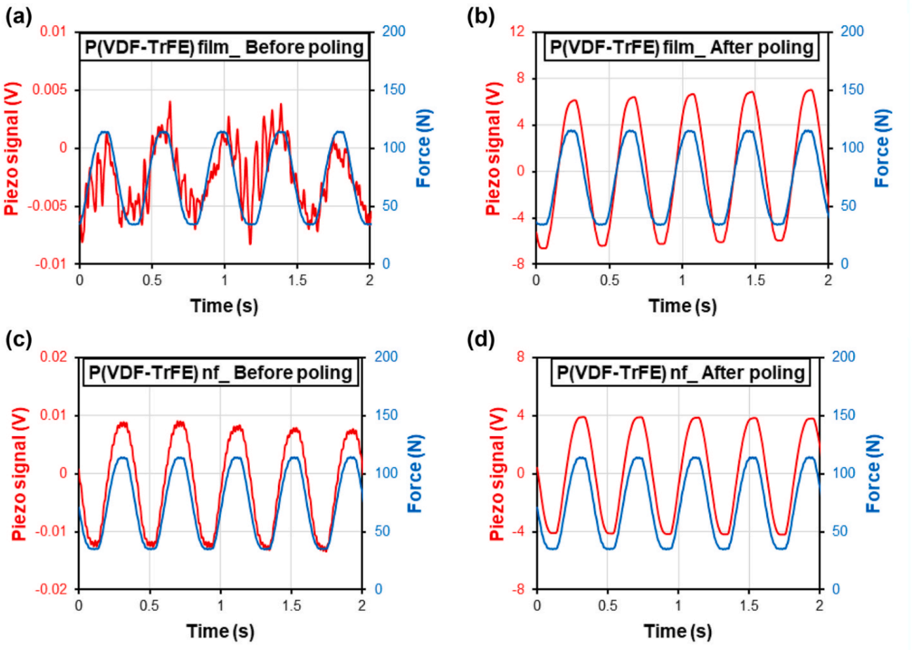

Fig. A.1. a) Piezoelectric signal of P(VDF-TrFE) thin film before and b) after poling (T = 30 °C, $D_{gg} = 5$ mm, $D_{ng} = 30$ mm, $V_g = 4$ kV, $V_n = 20$ kV). c) Piezoelectric signal of P(VDF-TrFE) nanofibers before and d) after poling (T = 130 °C, $D_{gg} = 5$ mm, $D_{ng} = 30$ mm, $V_g = -3$ kV, $V_n = -28$ kV).

Table A.1
Piezoelectric properties of the P(VDF-TrFE) film and nanofibers before and after corona poling.

	P(VDF-TrFE) film		P(VDF-TrFE) nanofibers	
	Before poling	After poling	Before poling	After poling
V_{pp} (V)	15.1×10^{-3}	12.5	26.4×10^{-3}	8.4
Sensitivity (mV N^{-1})	0.19	154.1	0.33	104.5
d_{33} (pC N^{-1})	17×10^{-3}	23.0	9.9×10^{-3}	−20.8

Accelerated life cycle fatigue tests were performed on the same specimens, with the aforementioned setup. The compressive force was oscillating between 0 N and 80 N with a frequency of 10 Hz, and the total amount of cycles is equal of 10^5. As observable from the graphs of Figure A.2a, the sensitivity of the piezoelectric film decreased from 154.1 mV N^{-1} to 148.4 mV N^{-1}, which corresponds to a decrease of 3.7% for the P(VDF-TrFE) film. In the case of P(VDF-TrFE) nanofibers, a decrease of 6.2% was measured after 10^5 cycles (Figure A.2b).

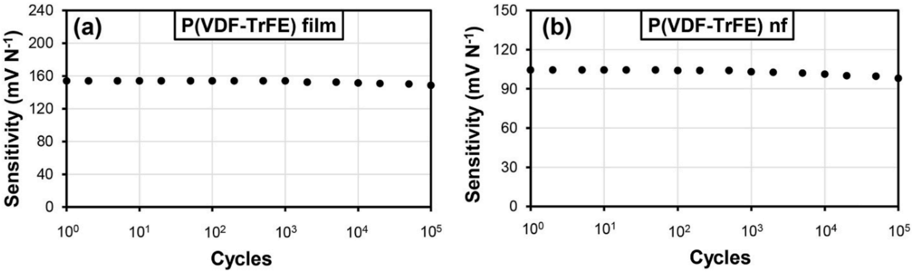

Fig. A.2. Accelerated fatigue cycle tests for a) P(VDF-TrFE) film and b) nanofibers.

Appendix B

FTIR spectroscopy was performed to determine the β-phase content of the samples before and after poling both for film and nanofibers, as shown in Figure B.1a and Figure B.1b, respectively. The β-phase content reported in Table B.1 has been calculated according to the following equation:

$$F(\beta) = \frac{A_\beta}{\left(\frac{K_\beta}{K_\alpha}\right) A_\alpha + A_\beta} \; x\,100\ (\%) \tag{B.1}$$

where A_β and A_α are the absorbance values at 840 cm^{-1} and 766 cm^{-1}, related to the β and α phase, respectively, while K_β and K_α are equal to 7.7 × 10^4 cm^2 mol^{-1} 6.1 × 10^4 and cm^2 mol^{-1}, and refer to the absorbance at the same wavelength of the characteristic phase. According to literature, the peaks at 841, 880, 1072, 1180, 1285, 1398 and 1431 cm^{-1} are the one related to the β phase [60–62], while the peak at 1123 cm^{-1} is related to the TrFE content [61].

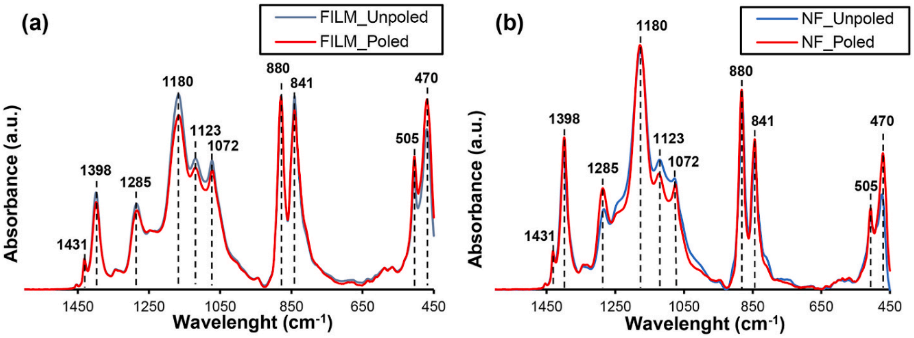

Fig. B.1. FTIR spectra of a) P(VDF-TrFE) films and b) nanofibers before and after poling.

The WAXD analyses were performed to determine the crystalline fractions of the samples before and after poling both for film and nanofibers, as shown in Figure B.2a and Figure B.2b, respectively. The crystalline fraction (χ_c) was calculated using the ratio of the integrated crystalline peaks and the total area of the crystalline peaks (A_c) and the amorphous halo (A_a), as in the following equation:

$$\chi_c = \frac{A_c}{A_c + A_a} \; x\,100\ (\%) \tag{B.2}$$

The diffractograms were analyzed with Fityk software to quantify the relative areas of the crystalline peak and the amorphous halo, ensuring accurate determination of the crystalline fraction. The values reported in Table B.1 show an increase of χ_c after the poling process, especially in the case of P(VDF-TrFE) nanofibers.

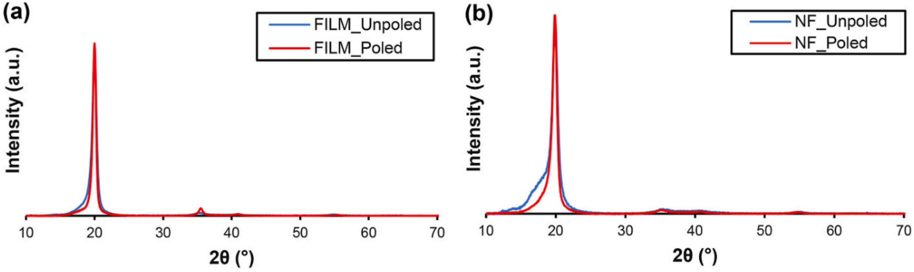

Fig. B.2. WAXD diffractograms of a) P(VDF-TrFE) films and b) nanofibers before and after poling.

Table B.1
β-phase content crystalline fractions of the samples before and after poling, both for film and nanofibers.

	P(VDF-TrFE) film		P(VDF-TrFE) nanofibers	
	Before poling	After poling	Before poling	After poling
$F(\beta)$ (%)	90.3	90.4	91.4	94.1
X_C (%)	70.8	77.4	43.5	72.2

References

[1] Y.S. Rim, S.H. Bae, H. Chen, N. De Marco, Y. Yang, Recent progress in materials and devices toward printable and flexible sensors, Adv. Mater. 28 (2016) 4415–4440, https://doi.org/10.1002/adma.201505118.

[2] A.S. Farooq, P. Zhang, A comprehensive review on the prospects of next-generation wearable electronics for individualized health monitoring, assistive robotics, and communication, Sensors Actuators A Phys 344 (2022) 113715, https://doi.org/10.1016/j.sna.2022.113715.

[3] M. Dulal, M.R. Islam, S. Maiti, M.H. Islam, I. Ali, A.M. Abdelkader, K.S. Novoselov, S. Afroj, N. Karim, Smart and multifunctional fiber-reinforced composites of 2D heterostructure-based textiles, Adv. Funct. Mater. 33 (2023) 1–13, https://doi.org/10.1002/adfm.202305901.

[4] Y. Wu, Y. Ma, H. Zheng, S. Ramakrishna, Piezoelectric materials for flexible and wearable electronics: a review, Mater. Des. 211 (2021) 110164, https://doi.org/10.1016/j.matdes.2021.110164.

[5] S. Das Mahapatra, P.C. Mohapatra, A.I. Aria, G. Christie, Y.K. Mishra, S. Hofmann, V.K. Thakur, Piezoelectric materials for energy harvesting and sensing applications: roadmap for future smart materials, Adv. Sci. 8 (2021), https://doi.org/10.1002/advs.202100864.

[6] M.S. Vijaya, Piezoelectric materials and devices applications in engineering and medical sciences. http://link.springer.com/10.1007/978-3-540-77304-7, 2008.

[7] M. Serridge, T.R. Licht, Accelerometers piezoelectric and vibration preamplifiers. Theory and Application Handbook, 1987, p. 151.

[8] A. Huijer, C. Kassapoglou, L. Pahlavan, Acoustic emission monitoring of carbon fibre reinforced composites with embedded sensors for in-situ damage identification, Sensors 21 (2021), https://doi.org/10.3390/s21206926.

[9] M. Saeedifar, J. Mansvelder, R. Mohammadi, D. Zarouchas, Using passive and active acoustic methods for impact damage assessment of composite structures, Compos. Struct. 226 (2019) 111252, https://doi.org/10.1016/j.compstruct.2019.111252.

[10] M.E. Gino, G. Selleri, D. Cocchi, T.M. Brugo, N. Testoni, L. De Marchi, A. Zucchelli, D. Fabiani, M.L. Focarete, On the design of a piezoelectric self-sensing smart composite laminate, Mater. Des. 219 (2022) 110783, https://doi.org/10.1016/j.matdes.2022.110783.

[11] S.S. Won, M. Kawahara, C.W. Ahn, J. Lee, J. Lee, C.K. Jeong, A.I. Kingon, S. Kim, Lead-free Bi0.5(Na0.78K0.22)TiO3 nanoparticle filler–elastomeric composite films for paper-based flexible power generators, Adv. Electron. Mater. 6 (2020) 1–10, https://doi.org/10.1002/aelm.201900950.

[12] R. Dallaev, T. Pisarenko, D. Sobola, F. Orudzhev, S. Ramazanov, T. Trčka, Brief review of PVDF properties and applications potential, Polymers 14 (2022) 1–29, https://doi.org/10.3390/polym14224793.

[13] W. Zeng, W. Deng, T. Yang, S. Wang, Y. Sun, J. Zhang, X. Ren, L. Jin, L. Tang, W. Yang, Gradient CNT/PVDF piezoelectric composite with enhanced force-electric coupling for soccer training, Nano Res. 16 (2023) 11312–11319, https://doi.org/10.1007/s12274-023-5869-6.

[14] H. Bao, Y. Ma, J. Sun, Q. Zhao, L. Yang, Y. Hou, H. He, H. Huang, H. Ji, J. Qiu, Flexible and transparent ionic liquids/poly (vinylidene fluoride) composition-gradient piezo-active composites for highly sensitive pressure sensor, Adv. Electron. Mater. 9 (2023) 13, https://doi.org/10.1002/aelm.202201013.

[15] J. Deng, Q. Sun, Z. Wu, Y. Wang, Enhanced self-driven flexible piezoelectric nanogenerator sensor based on NaNbO3/P(VDF-TrFE) films for security applications, Surf. Interfaces 53 (2024) 105001, https://doi.org/10.1016/j.surfin.2024.105001.

[16] J. Deng, P. Zhao, Z. Wu, Y. Wang, Optimized performance of self-driven piezoelectric sensors through KNN/Nb2CTx synergistic effect, Ceram. Int. 50 (2024) 31154–31163, https://doi.org/10.1016/j.ceramint.2024.05.421.

[17] J. Yang, Q. Chen, F. Xu, H. Jiang, W. Liu, X. Zhang, Z. Jiang, G. Zhu, Epitaxy enhancement of piezoelectric properties in P (VDF-TrFE) copolymer films and applications in sensing and energy harvesting, Adv. Electron. Mater. 6 (2020) 1–13, https://doi.org/10.1002/aelm.202000578.

[18] S. Sriphan, N. Vittayakorn, Hybrid piezoelectric-triboelectric nanogenerators for flexible electronics: recent advances and perspectives, J. Sci. Adv. Mater. Devices 7 (2022) 100461, https://doi.org/10.1016/j.jsamd.2022.100461.

[19] J. Park, Y. won Lim, S.Y. Cho, M. Byun, K. Il Park, H.E. Lee, S.D. Bu, K.T. Lee, Q. Wang, C.K. Jeong, Ferroelectric polymer nanofibers reminiscent of morphotropic phase boundary behavior for improved piezoelectric energy harvesting, Small 18 (2022) 1–12, https://doi.org/10.1002/smll.202104472.

[20] G. Selleri, F. Mongioì, E. Maccaferri, R. D'Anniballe, L. Mazzocchetti, R. Carloni, D. Fabiani, A. Zucchelli, T.M. Brugo, Self-sensing soft skin based on piezoelectric nanofibers, Polymers 15 (2023) 1–14, https://doi.org/10.3390/polym15020280.

[21] U. Pierre Claver, G. Zhao, Recent progress in flexible pressure sensors based electronic skin, Adv. Eng. Mater. 23 (2021) 1–17, https://doi.org/10.1002/adem.202001187.

[22] A. Closson, H. Richards, Z. Xu, C. Jin, L. Dong, J.X.J. Zhang, Method for Inkjet-printing PEDOT:PSS polymer electrode arrays on piezoelectric PVDF-TrFE fibers, IEEE Sens. J. XX (2021), https://doi.org/10.1109/JSEN.2021.3071321.

[23] X. Wang, F. Sun, G. Yin, Y. Wang, B. Liu, M. Dong, Tactile-sensing based on flexible PVDF nanofibers via electrospinning: a review, Sensors 18 (2018), https://doi.org/10.3390/s18020330.

[24] G. Selleri, F. Grolli, M.R. Randi, E. Maccaferri, T.M. Brugo, G. Valdrè, A. Zucchelli, D. Fabiani, Composite material based on piezoelectric core-shell nanofibers for tactile recognition, Composites, Part B 280 (2024), https://doi.org/10.1016/j.compositesb.2024.111494.

[25] G. Selleri, M.E. Gino, T.M. Brugo, R. D'Anniballe, J. Tabucol, M.L. Focarete, R. Carloni, D. Fabiani, A. Zucchelli, Self-sensing composite material based on piezoelectric nanofibers, Mater. Des. 219 (2022), https://doi.org/10.1016/j.matdes.2022.110787.

[26] W. Deng, T. Yang, L. Jin, C. Yan, H. Huang, X. Chu, Z. Wang, Cowpea-structured PVDF/ZnO nano fi bers based fl exible self-powered piezoelectric bending motion sensor towards remote control of gestures, Nano Energy 55 (2019) 516–525.

[27] L. Gasperini, G. Selleri, D. Fabiani, Highly sensitive piezoelectric ceramic nanofibers for flexible transducers and advanced applications, Proc. 2024 IEEE 5th Int. Conf. Dielectr. ICD 2024 (2024) 1–4, https://doi.org/10.1109/ICD59037.2024.10613172.

[28] F. Mongioì, G. Selleri, E. Maccaferri, D. Fabiani, A. Zucchelli, T.M. Brugo, CFRP laminate with autonomous sensing and enhanced impact resistance by P(VDF-TrFE) nanofibers interleaving, Composites, Part B 293 (2025) 112143, https://doi.org/10.1016/j.compositesb.2025.112143.

[29] T.M. Brugo, E. Maccaferri, D. Cocchi, L. Mazzocchetti, L. Giorgini, D. Fabiani, A. Zucchelli, Self-sensing hybrid composite laminate by piezoelectric nanofibers interleaving, Composites, Part B 212 (2021) 108673, https://doi.org/10.1016/j.compositesb.2021.108673.

[30] H.L.W. Chan, Z. Zhao, K.W. Kwok, C.L. Choy, C. Alquié, C. Boué, J. Lewiner, Polarization of thick polyvinylidene fluoride/trifluoroethylene copolymer films, J. Appl. Phys. 80 (1996) 3982–3991, https://doi.org/10.1063/1.363356.

[31] G. Eberle, E. Bihler, W. Eisenmenger, Polarization dynamics of VDF-TrFE copolymers, IEEE Trans. Electr. Insul. 26 (1991) 69–77, https://doi.org/10.1109/14.68230.

[32] G. Selleri, L. Gasperini, L. Piddiu, D. Fabiani, Comparison between AC and DC polarization methods of piezoelectric nanofibrous layers, in: 2022 IEEE 4th Int. Conf. Dielectr., 2022, https://doi.org/10.1109/ICD53806.2022.9863546.

[33] J. Choi, H. Kim, S. Yoon, C.K. Jeong, Quest for comparing direct-current (DC) and alternating-current (AC) poling effects on ferroelectric and piezoelectric materials, J. Korean Inst. Electr. Electron. Mater. Eng. 37 (2024) 563–581.

[34] T.M. Brugo, E. Maccaferri, D. Cocchi, L. Mazzocchetti, L. Giorgini, D. Fabiani, A. Zucchelli, Self-sensing hybrid composite laminate by piezoelectric nanofibers interleaving, Composites, Part B 212 (2021) 108673, https://doi.org/10.1016/j.compositesb.2021.108673.

[35] Y.M. Yousry, K. Yao, S. Chen, W.H. Liew, S. Ramakrishna, Mechanisms for enhancing polarization orientation and piezoelectric parameters of PVDF nanofibers, Adv. Electron. Mater. 4 (2018) 1–8, https://doi.org/10.1002/aelm.201700562.

[36] G. Selleri, M.E. Gino, L. Gasperini, M. Zanoni, C. Gualandi, M.L. Focarete, D. Fabiani, Study on the polarization process for piezoelectric nanofibrous layers, in: Annu. Rep. - Conf. Electr. Insul. Dielectr. Phenomena, CEIDP 2021-Decem, 2021, pp. 61–64, https://doi.org/10.1109/CEIDP50766.2021.9705470.

[37] J.A. Giacometti, O.N. Oliveira, Corona charging of polymers, IEEE Trans. Electr. Insul. 27 (1992) 924–943, https://doi.org/10.1109/14.256470.

[38] A. Salimi, A.A. Yousefi, Conformational changes and phase transformation mechanisms in PVDF solution-cast films, J. Polym. Sci., Part B: Polym. Phys. 42 (2004) 3487–3495, https://doi.org/10.1002/polb.20223.

[39] B. Mohammadi, A.A. Yousefi, S.M. Bellah, Effect of tensile strain rate and elongation on crystalline structure and piezoelectric properties of PVDF thin films, Polym. Test. 26 (2007) 42–50, https://doi.org/10.1016/j.polymertesting.2006.08.003.

[40] J. Yadong, Y. Yun, Y. Junsheng, W. Zhiming, L. Wei, X. Jianhua, X. Guangzhong, Study of thermally poled and corona charged poly(vinylidene fluoride) films, Polym. Eng. Sci. (2007) 1–10, https://doi.org/10.1002/pen.

[41] A. Sasmal, S. Sen, P.S. Devi, Frequency dependent energy storage and dielectric performance of Ba-Zr Co-doped BiFeO3loaded PVDF based mechanical energy harvesters: effect of corona poling, Soft Matter 16 (2020) 8492–8505, https://doi.org/10.1039/d0sm01031f.

[42] D. Waller, A. Safari, Corona poling of pzt ceramics and flexible piezoelectric composites, Ferroelectrics 87 (1988) 189–195, https://doi.org/10.1080/00150198808201381.

[43] H. Cui, R. Hensleigh, D. Yao, D. Maurya, P. Kumar, M.G. Kang, S. Priya, X. Rayne Zheng, Three-dimensional printing of piezoelectric materials with designed anisotropy and directional response, Nat. Mater. 18 (2019) 234–241, https://doi.org/10.1038/s41563-018-0268-1.

[44] H. Wang, J. Liu, S. Sadeghzade, R. Hou, H. Yuan, Improved corona discharge-based modified poling method for 0–3 PZT/PEGDA piezoelectric composites, Ceram. Int. 49 (2023) 11334–11343, https://doi.org/10.1016/j.ceramint.2022.11.333.

[45] S.K. Mahadeva, J. Berring, K. Walus, B. Stoeber, Effect of poling time and grid voltage on phase transition and piezoelectricity of poly(vinyledene fluoride) thin films using corona poling, J. Phys. D Appl. Phys. 46 (2013), https://doi.org/10.1088/0022-3727/46/28/285305.

[46] J.A. Giacometti, S. Fedosov, M.M. Costa, Corona charging of polymers: recent advances on constant current charging, Braz. J. Phys. 29 (1999) 269–279, https://doi.org/10.1590/S0103-97331999000200009.

[47] J.A. Giacometti, J. Sinézio Carvalho Campos, Constant current corona triode with grid voltage control. Application to polymer foil charging, Rev. Sci. Instrum. 61 (1990) 1143–1150, https://doi.org/10.1063/1.1141438.

[48] Y. Li, W. Feng, L. Meng, K.M. Tse, Z. Li, L. Huang, Z. Su, S. Guo, Investigation on in-situ sprayed, annealed and corona poled PVDF-TrFE coatings for guided wave-based structural health monitoring: from crystallization to piezoelectricity, Mater. Des. 199 (2021) 109415, https://doi.org/10.1016/j.matdes.2020.109415.

[49] J.-Y. Ke, H.-J. Chu, Y.-H. Hsu, C.-K. Lee, A highly flexible piezoelectret-fiber pressure sensor based on highly aligned P(VDF-TrFE) electrospun fibers, Act, Passiv. Smart Struct. Integr. Syst. 10164 (2017) (2017), https://doi.org/10.1117/12.2259854, 101642X.

[50] M.A. Barique, Y. Neo, M. Noyori, L. Aprila, M. Asai, H. Mimura, A large piezoelectric response in highly-aligned electrospun poly(vinylidene fluoride/trifluoroethylene) nanofiber webs for wearable energy harvesting, Nanotechnology 32 (2021), https://doi.org/10.1088/1361-6528/abb5d3.

[51] C.X.J. Yi, Y. Song, S. Zhang, Z. Cao, C. Li, Corona − poled porous electrospun films of gram − scale Y − doped ZnO and PVDF composites for piezoelectric nanogenerators, Polymers (2022).

[52] D.C. Montgomery, Design and Analysis of Experiments, 9 Edition, Wiley, 2017.

[53] J.A. Giacometti, Radial current-density distributions and sample charge uniformity in a corona triode, J. Phys. D Appl. Phys. 20 (1987) 675–682, https://doi.org/10.1088/0022-3727/20/6/001.

[54] M.S. Bendilmi, T. Zeghloul, Z. Ziari, K. Medles, L. Dascalescu, Experimental characterization of a tri-needle-type corona electrode in view of improving charging uniformity, IEEE Trans. Ind. Appl. 58 (2022) 783–791, https://doi.org/10.1109/TIA.2021.3130012.

[55] J.W. Zhang, Y.C. Cui, C. Putson, R.T. Liu, C.L. Liu, Surface charge accumulation effect of polyimide after temperature controlling corona polarization, Proc. 2016 IEEE Int. Conf. Dielectr. ICD 2 (2016) (2016) 1151–1154, https://doi.org/10.1109/ICD.2016.7547821.

[56] A. Bendaoud, A. Tilmatine, K. Medles, M. Rahli, M. Huzau, L. Dascalescu, Characterization of dual corona-electrostatic electrodes for electrostatic processes applications, IEEE Trans. Ind. Appl. 44 (2008) 692–698, https://doi.org/10.1109/TIA.2008.921376.

[57] A. Bouteffaha, A. Bendaoud, A. Tilmatine, K. Medles, M. Plopeanu, L. Dascalescu, Experimental and numerical characterization of corona discharge generated by a triode electrode system, in: 2013 IEEE Ind. Appl. Soc. Annu. Meet, IEEE, 2013, pp. 1–6.

[58] L. Dascalescul, A. Samuilal, D. Rafiroiul, R. Mora, Multiple-needle corona electrodes for electrostatic processes application, IEEE Ind. Appl. Soc. (1997).

[59] L. Gasperini, A. Rumi, G. Selleri, D. Fabiani, P. Seri, Optimization of corona triode polarization by 2D electrostatic mapping, IEEE Conf. Electr. Insul. Dielectr. Phenom. (2023) 1–4.

[60] J.S. Andrew, D.R. Clarke, Enhanced ferroelectric phase content of polyvinylidene difluoride fibers with the addition of magnetic nanoparticles, Langmuir 24 (2008) 8435–8438, https://doi.org/10.1021/la801617q.

[61] A. Arrigoni, L. Brambilla, C. Bertarelli, G. Serra, M. Tommasini, C. Castiglioni, P (VDF-TrFE) nanofibers: structure of the ferroelectric and paraelectric phases through IR and Raman spectroscopies, RSC Adv. 10 (2020) 37779–37796, https://doi.org/10.1039/d0ra05478j.

[62] L. Persano, C. Dagdeviren, Y. Su, Y. Zhang, S. Girardo, D. Pisignano, Y. Huang, J. A. Rogers, High performance piezoelectric devices based on aligned arrays of nanofibers of poly(vinylidenefluoride-co-trifluoroethylene), Nat. Commun. 4 (2013) 1610–1633, https://doi.org/10.1038/ncomms2639.